Since January 2020 Elsevier has created a COVID-19 resource centre with free information in English and Mandarin on the novel coronavirus COVID-19. The COVID-19 resource centre is hosted on Elsevier Connect, the company's public news and information website.

Powder Technology 390 (2021) 174–181

Contents lists available at ScienceDirect

Powder Technology

journal homepage: www.elsevier.com/locate/powtec

Automatic 3D cluster modelling of COVID-19 through voxel-based redistribution

Mingzhi Wang [a,b,c,*], Yushi Liu [a,b,c], Beimeng Qi [d,*], Wei Wang [a,b,c]

[a] School of Civil Engineering, Harbin Institute of Technology, Harbin 150090, China
[b] Key Lab of Structures Dynamic Behavior and Control of the Ministry of Education, Harbin Institute of Technology, Harbin 150090, China
[c] Key Lab of Smart Prevention and Mitigation of Civil Engineering Disasters of the Ministry of Industry and Information Technology, Harbin Institute of Technology, Harbin 150090, China
[d] College of Quality & Safety Engineering, China Jiliang University, Hangzhou 310018, China

ARTICLE INFO

Article history:
Received 28 September 2020
Received in revised form 6 May 2021
Accepted 23 May 2021
Available online 25 May 2021

Keywords:
Voxel-based computation
Particle distribution simulation
COVID-19
Irregular-shaped particle
Representative elementary volume

ABSTRACT

Computational analysis of virus dynamics provides a non-contact environment for the study of the vital object. Cluster modelling is an essential step to investigate the properties of a group of viruses, and an automatic approach is required for massive 3D data processing. The morphological complexity of individual virus limits the application of smooth function algorithms with a regular-shaped assumption. This paper proposed a voxel-based redistribution approach to generate the virus cluster with COVID-19 input automatically. Representative elementary volume analysis was performed to address the statistical influence from the digital sample size. Coordination number analysis and surface density measurement were conducted with COVID-19 input and spherical input for comparison. The proposed approach is in natural compatibility with the lattice Boltzmann method for fluid dynamics analysis. A virtual permeation simulation was performed with the COVID-19 cluster and spherical cluster to demonstrate the necessity to include spike protein structure in the cluster modelling.

1. Introduction

In 2019 a global pandemic with the COVID-19 virus attacked the human race, and the impact on the scientific community was beyond the academic disciplines [1,2]. Contribution from various fields of study was in need to overcome the suddenly emerged topic. In computational powder technology, particle redistribution is a continuously studied issue with a recorded history of development [3–5]. By treating each virus as an individual particle, the virus cluster formation can be realized for large-scale virus dynamics analysis [6]. More recently, the reconstruction of the individual COVID-19 model promptly fulfilled the requirement for further cluster modelling [7]. Hence, particle-based simulation to describe the 3D spatial distribution of the virus cluster become the next essential step for analysis with a group of viruses. The available solutions for particle cluster formation are the discrete element method (DEM) [8] and the computational molecular dynamics (MD) [9]. The above methods essentially require a continuous description of the viruses particle with a smooth analytical geometry function. Therefore, the complexity of the particle morphology become one major restriction for the rapid modelling of an urgent problem. In the previous study, the spherical assumption was widely adopted to simulate the particle redistribution in general [10], and discussion has extended to other regular-shaped particles, including column [11], elliptic [12] and polygon [13]. MD solution also adopted the spherical assumption, but intermolecular bonding was introduced [14]. More recently, the application image-based input has been brought into discussion for spherical [15] and non-spherical particles [16]. The above work suggests adopting a 3D realistic image of a particle in a cluster creation algorithm. In terms of the cluster modelling of COVID-19, the surface structure of an individual virus consist of spike protein, envelop protein and membrane [17]. The complexity of the virus morphology is beyond the previously discussed model, and an alternative approach is required to perform the automatic redistribution.

Simultaneous to the methodology with a smooth function, the discrete branch of the particle distribution algorithms are the 3D voxel-based methods [18,19] developed from 2D pixel-based approaches [20]. The most outstanding feature of the discrete methods is the feasibility to model arbitrary-shape particle since the redistribution system was described with discrete matrix instead of analytical geometry. Competition exists between voxel-based approaches and smooth function approaches. The main argument raised by the latter is that the first principles it claims to follow are more valid than the stochastic interpretation in the former [21]. However, the fact is that the Newtonian coefficients in a practical problem are often not confirmative, including but not limit to the attractive potential coefficient [22], pairwise interactions coefficient [23], damping coefficient [24] and elastic modulus [25]

* Corresponding authors at: School of Civil Engineering, Harbin Institute of Technology, Harbin 150090, China.
E-mail addresses: mwang@hit.edu.cn (M. Wang), qbm@cjlu.edu.cn (B. Qi).

https://doi.org/10.1016/j.powtec.2021.05.083
0032-5910/

Nomenclature and abbreviation

Terms	Description
COVID-19	A global pandemic outbroke in 2019
Molecular dynamics (MD)	A computational algrithm to simulate the movement of molecular particles.
Discrete element method (DEM)	A computation algorithm to simulate the movement of general particles with contact mechanics
Cellular automata (CA)	A series of computational algorithms to model global behaviour from individual cells.
Lattice gas automata (LGA)	A cellular automaton to simulate microscopic fluid behaviour.
Lattice Boltzmann method (LBM)	A computational algorithm to simulate mesoscopic and microscopic fluid behaviour.
Representative elementary volume (REV)	The minimum volume over which the measurement of global properties can be representative.
DxQy	A matrix description term originated from the Lattice Boltzmann method, where the lattice system was described with x dimensions and y directions of velocities.
Voxel	A unit volume of the 3D volumetric data, corresponding to one cell in cellular automata.

from microscale to macroscale. Hence, the fundamental elements of the claimed first principle were partially supplemented with judgement and calibration [26].

On the other hand, a collaborative integration of the voxel-based and smooth function approaches is possible by combining the stochastic and analytical steps [19,27,28]. More importantly, the mainstream images of 3D biological structures captured in a computer are in the forms of voxels (vertex) [29], which are in natural compatibility with voxel-based redistribution approaches. To sum, the analytical geometry and first-principal requirement for smooth function methods restrict the timely application of the strategies to model the COVID-19 cluster. The arbitrary-shape adaptability and biological image compatibility make the voxel-based approaches more suitable to offer the automatic modelling of the virus cluster before the academic establishment of the virus first principle.

Automatic modelling with a computer is originated from the binary calculation in a discrete form such as cellular automaton (CA) [30]. In computational fluid dynamics (CFD), the lattice Boltzmann method (LBM) is a series of algorithms developed through the bloodline of Boltzmann Eq. [31], CA [32], lattice gas automata (LGA) [33] and LBM [34]. The same philosophy of discrete computation supports the development of the CA, LGA, LBM, voxel-based redistribution and 3D imaging, as mentioned above. Mathematically, the voxel-based approaches' compatibility results from the application of matrix as the fundamental unit of calculation. Therefore, it is feasible to unify the voxel-based redistribution and LBM fluid dynamics analysis without error-causing data conversion. In a cluster modelling with numerous viruses, the digital sampling of a cluster will have a statistical influence on the macroscopic property [35]. Hence, representative elementary volume (REV) analysis is necessary to determine the sample size before the computational analysis [36]. Through cluster modelling of the COVID-19 virus in REV, a mesoscopic investigation is numerically enabled for a more comprehensive understanding of the particle system.

This study aims to provide a numerical modelling approach to simulate the spatial distribution of the virus group until the discovery of the first principle. REV analysis was performed to determine the representative size of the digital cluster before in-depth analysis. Coordination number analysis and virtual permeation analysis were performed to determine the effect of including spike protein structure in cluster modelling. The virtual permeation analysis also demonstrates compatibility between the voxel-based redistribution and lattice Boltzmann CFD. The importance of spike protein is emphasized with a comparison between the COVID-19 cluster and the spherical cluster. The influence of virus interconnection and surface density was discussed for the potential application of the technique in mesoscopic pathology.

2. Methodology

2.1. Overview, voxelization and registration

Fig. 1(a) presents the overview flowchart of this work. The corresponding process was generalized into a sequence of individual particle input, spatial redistribution, REV determination, cluster extraction and analysis. The extracted volume of the COVID-19 cluster is the target for further morphological and CFD analysis. The biological structure of an individual virus is obtained from the United States Department of Health and Human Services under the creative commons (CC) license [37]. The 3D image data was then digitized into voxels, as illustrated by Fig. 1(b). The mean particle size of the virus was reported to be 67 nm [38]. During the digitization, the outer surface of the biological model was registered as membrane zone and spike zone, respectively. The voxelization step is essential to perform voxel-based redistribution, and the registration step is prepared to isolate all the spike protein in the virus cluster. The digitization was realized by extracting the point data of the .stl file provided by the US Department of Health and

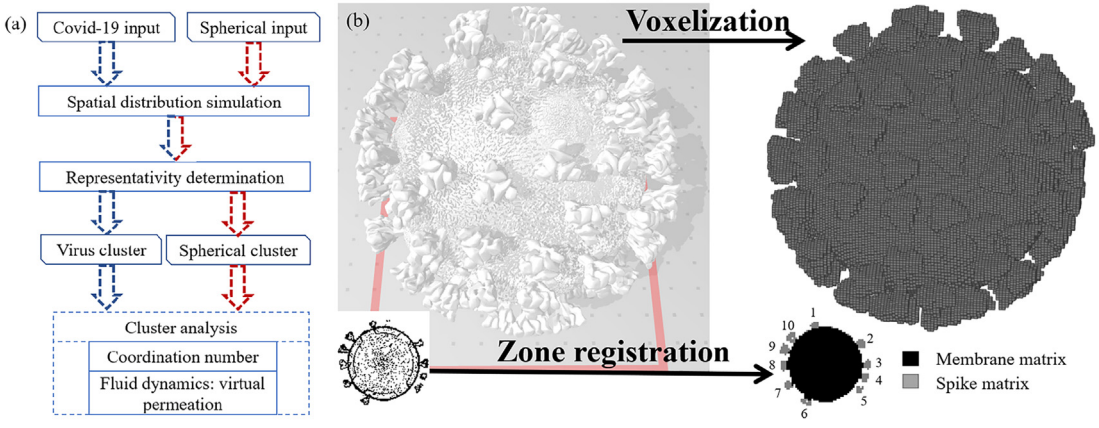

Fig. 1. (a) Flowchart of the computational framework. (b) The voxelization of an individual virus.

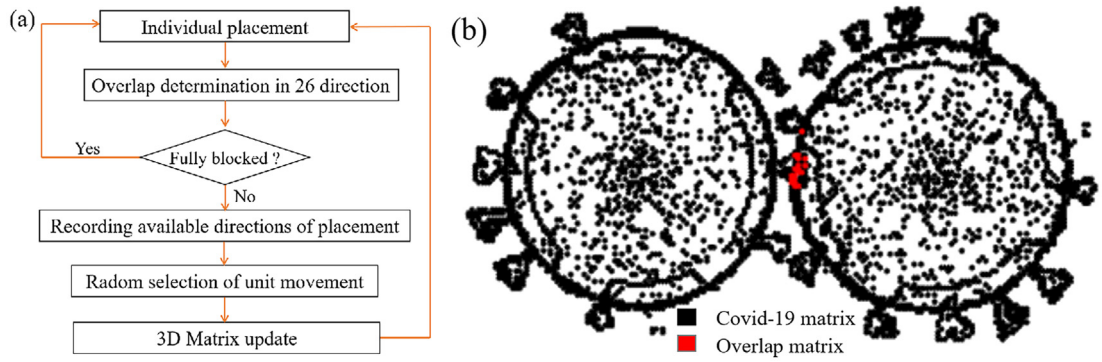

Fig. 2. (a) The program for automatic cluster modelling. (b) Contact determination of viruses in contact.

Human Services. The length mapping was discretized by averaging the continuous point value to a discrete target voxel.

The segmentation of the spike protein was realized with the following step. Firstly, locate the centroid coordinate of the single virus model. Secondly, use the centroid coordinate as the centre of a growing sphere. Thirdly, continually increasing the radius of the sphere. Fourthly, recording the overlap between the single virus and the sphere until a sudden drop of the overlapping volume. Fifthly, remove the sphere volume from the single virus. The above step resulted in a rough location of the spike protein. More precise propein spikes matrixes were extracted by removing the volume, which was significantly lower than the rest. The isolation of individual spike protein was then performed without spike interconnection.

2.2. Voxel-based redistribution

The 3D voxelized COVID-19 image was then inputted into the redistribution program. The redistribution process was realized by repeatedly adjusting the position of each virus until a user-specified volumetric fraction was reached. A preliminary step was performed before the volume densification, which is described as follow. Initially, one individual virus was located in a 3D matrix of zeros by changing the occupied elements to be ones. Repeating the assignment of the individual virus without overlapping then form a loose cluster floating in the volume. Afterwards, the redistribution program, as demonstrated by Fig. 2 (a), was initiated. Firstly, D3Q27 neighbours [39] or 3D Moore neighbourhood [40] of one virus was extracted and added to the cluster matrix. The overlap of unit movement was then determined, as illustrated in Fig. 2(b). If the rest of the viruses blocked all the 26 directions of movement, the current virus was immobilized until the next loop of iteration. Otherwise, the available directions of the one-voxel movement were recorded as possible movement directions. Secondly, a random choice of possible directions was performed to execute the movement. In order to simulate the gravitational environment, the downwards probability is assigned to be 25% higher than the rest of the directions. Finally, the cluster matrix was updated with the new position of the virus, and a new iteration was initiated. The fundamental methodology of the proposed program can be categorized into the cellular automaton philosophy from John von Neumann [30], who lay the foundation of modern computation. The proposed algorithm reflects the philosophy that each virus is a machine with automatic rules to find its position in a densified space. The compatibility between image processing techniques and voxel-based distribution is originated from the same principle of matrix operation. The first author of this paper wrote the programme of this paper with GNU Octave. [41]

2.3. Representativity determination

The sampling size strongly influences the measured properties of a heterogeneous structure. Representative elementary volume is defined as the volume larger than which the local heterogeneity minorly affects the morphological measurement. The determination of representative elementary volume is essential to guarantee the modelling representativity with the highest computational efficiency. Statistically, the Chi-square criterion provided a quantitative standard to evaluate the sample size as given by Eq. 1. The phase of interest in this study is the virus cluster.

$$\epsilon^2 = \sum_{i=1}^{n} \frac{(S_i - <S>)^2}{<S>} \tag{1}$$

where ϵ^2 is the chi-square coefficient, S_i is the volumetric fraction of the virus cluster, $<S>$ is the mean of S_i, n is the number of samples with the same sample size. In this study, $n = 8$ samples were extracted from the whole volume under each sample size. The representative threshold was assigned to be $\epsilon^2 < 7 \times 10^{-5}$.

2.4. Morphology analysis of the virus cluster

Morphological analysis with the COVID-19 redistribution was performed with coordination number analysis [42] and surface density measurement. Coordination number was defined as the number of contacts between one virus to the other virus. The computation of the individual coordination number was realized by counting the number of viruses that were in 3D connection with the target virus. By dividing the overall coordination number by the number of the target virus, the mean coordination number is therefore calculated. Surface density was defined as the amount of virus per unit lattice area (lu^2), where lu is a dimensionless length unit for individual voxel. The computation of the surface density is realized by dividing the overall number of viruses or sphere particles, which were in contact with the bottom surface, by the surface area. The length mapping of this study is 1.56 nm/lu.

2.5. Fluid dynamics through the virus cluster

The virtual permeability analysis adopted an established Lattice Boltzmann method (LBM) [43] for ultra-low porosity. The computation was realized by the non-commercial APMS-Permeation program reproduced from Dr. Wang's previous work [41], where details of the program and validation can be found in [44]. The essential formula for fluid permeation analysis is given by Eq. 2. [44]

$$K = \frac{v}{\Delta p_z} \cdot N_z \frac{\sum_{i=1}^{N_x} \sum_{j=1}^{N_y} \sum_{k=1}^{N_z} u_z(i,j,k)}{N_x \cdot N_y \cdot N_z \cdot} \tag{2}$$

where K is the intrinsic permeability, v is the dynamic viscosity of the fluid, Δp_z is the pressure difference between the top and bottom surface, $u_z(i,j,k)$ is the velocity weight in z^{th} direction at the coordinate of i, j and k, N_x, N_y and N_z are the directional number of voxels in x, y and z-direction, respectively.

The contribution of this paper is the voxel-based redistribution approach to model COVID-19 cluster. The application of APMS-Permeation demonstrates the compatibility of the proposed redistribution algorithm to computational fluid dynamics analysis. Due to the voxel-based nature of the proposed algorithm, the matrix data of the redistribution result can be directly applied to matrix-based LBM without any data conversion.

3. Result and discussion

3.1. Representative elementary volume for cluster analysis

A difference in 3D analysis between an individual virus and virus cluster is the statistical influence from the digital sample size. In terms of the cluster bahevior, a limited amount of viruses will lead to non-representative results. Fig. 3(a) presents the structural heterogeneity with virus volumetric fraction as the property of interest. The size ratio in the x-axis was defined as the ratio of virus size to volume size. Results in Fig. 3(a) shows that the statistical variance within the size ratio range of (0,10) is outstanding even before the quantitative evaluation. An upper phase fraction of 62% was obtained from the modelled virus cluster. A previous discovery [45] reported an upper phase fraction of 64% for contacted spherical-cluster, which was support by [46,47]. The REV analysis performed in this study was on a fixed cluster structure with overly large sample size. The constant property was reported to be the fractal dimension [15,16,28] for algorithms requiring growing particle size. However, the growth of primary particles can lead to inconstant REV.

In comparison, the REV-Loose curve resulted in a COVID-19 cluster with a phase fraction close to the spherical model. However, the reduction of the phase fraction was caused by the spike structure on the spherical surface. A more profound influence on the cluster behaviour exists beyond the volumetric properties. The comparison indicates that spike protein structure slightly amends the volumetric property of the clustering result from the spherical assumption. The comparison between the REV-Loose curve and REV-Dense suggests that the loosely distributed COVID-19 cluster requires a higher size ratio threshold for representativity. Fig. 3(b) further presents the Chi-square result as a quantitative evaluation of the representativity. The result indicates that a size ratio of 10 is sufficient to maintain the Chi-square value lower than the pre-defined threshold. As a result, the analysis with virus cluster in the following study adopted a size ratio of 10 during the digital sampling.

3.2. Visualized redistribution for computational purpose

The usage of 3D models of COVID-19 only for illustrative purpose is a tremendous waste of computational capability in current times. The visualized data provides a non-contact environment for physical and biological investigation. The essence of a cluster redistribution is the automatic modelling of the virus spatial arrangement with a tunable volumetric fraction. Fig. 4 demonstrate the visualized result of the proposed redistribution algorithm. A specific cluster arrangement was formed from loose distribution to dense distribution by controlling the iteration of densification. Fig. 4(a) presents the loosely distributed viruses with 0 densification iteration, corresponding to the floating COVID-19 upon the initial airborne spread. Fig. 4(b) shows the densely distributed viruses in a volume, corresponding to the high concentration scenario. Fig. 4(c) demonstrates the surface clusters extracted from the loose and dense redistribution, respectively. The visualized result shows the available arrangement from the digital redistribution, reflecting the control variable during a dynamics analysis requiring a 3D structure. Through the zone registration at the initial step of discretization, it becomes possible to isolate the spike protein structures from the whole cluster, as presented by Fig. 4(d). From a non-biological perspective, the spike protein is the major structural difference between a COVID-19 and a spherical particle. A continuous description of each spike on the virus membrane requires different sets of analytical geometry covering all the surface equations. In comparison, the voxel-based computation in this study demonstrates a feasible representation of various spikes in one 3D matrix. The sample zie of these clusters were 200 × 200 × 200 lu^3, which was converted to 312 × 312 × 312 nm^3.The structural separation between spike protein and the virus membrane allows further infection investigation in the mesoscale.

3.3. The influence of virus morphology

The spherical assumption is the most applied assumption to simulate particle redistribution. The simplicity of the analytical geometry ($r^2 = x^2 + y^2 + z^2$) makes the mathematical determination of inter-particle contact a straightforward comparison between the centre distance and the sum of the radius. Adopting the spherical assumption can preliminary model the virus cluster to some extend. However, it is a fact that the morphology of COVID-19 is different from the sphere. The virus cluster modelling assembles each particle's morphological difference, resulting in an enlarged error caused by local difference. Coordination number is a quantitative evaluation of the virus interconnection inside the virus cluster, which influences the infectivity and fatality from a pathological perspective.

Results in Fig. 5(a) shows that spikeless sphere input resulted in a mean coordination number of 6 within a range of (0,11), and a surface density measurement of 4.8611 × 10^{-4}/lu^2 was captured. The surface density indicates the amount of virus on the surface was 1.9974 × 10^{-4} per nm^2. In comparison, [42] reported a coordination number of 6 when the phase fraction was 64%. This result was in satisfactory

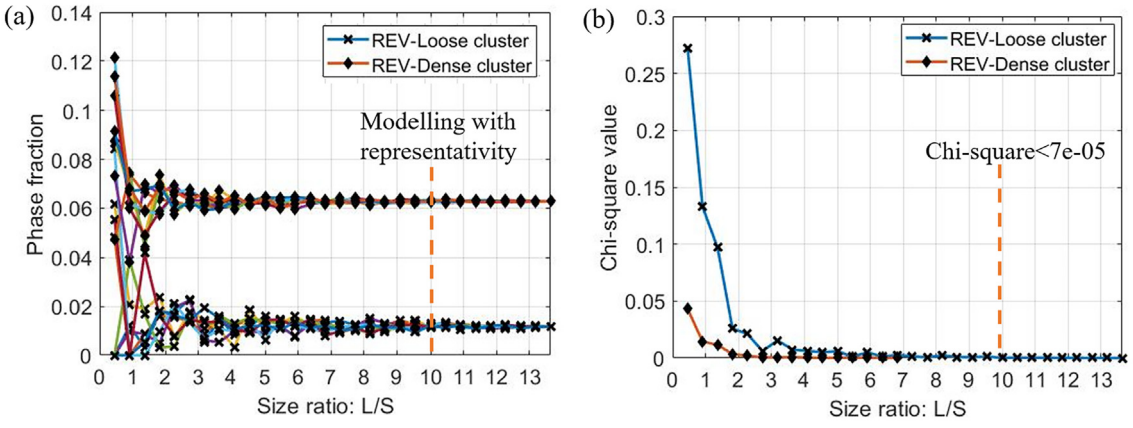

Fig. 3. (a) Statistical influnce from the size ratio. (b) Chi-square criterion to determine the digital sample size.

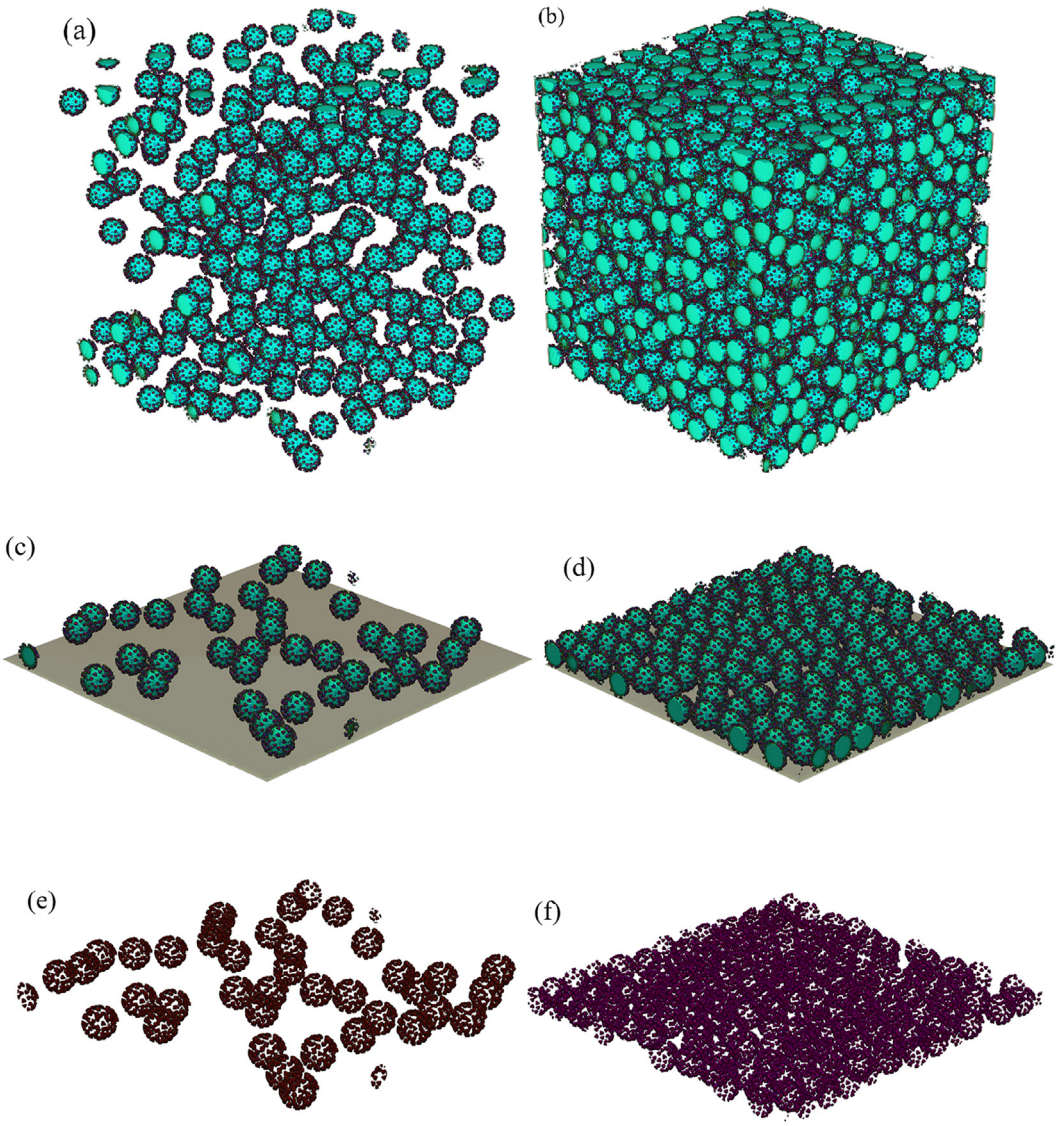

Fig. 4. (a) Loose redistribution of the viruses in a REV. (b) Dense redistribution of the viruses in REV. (c) Loose redistribution of the viruses on a surface. (d) Dense redistribution of the viruses on a surface. (e) Isolation of spike protein in the loose cluster. (f) Isolation of spike protein in the dense cluster.

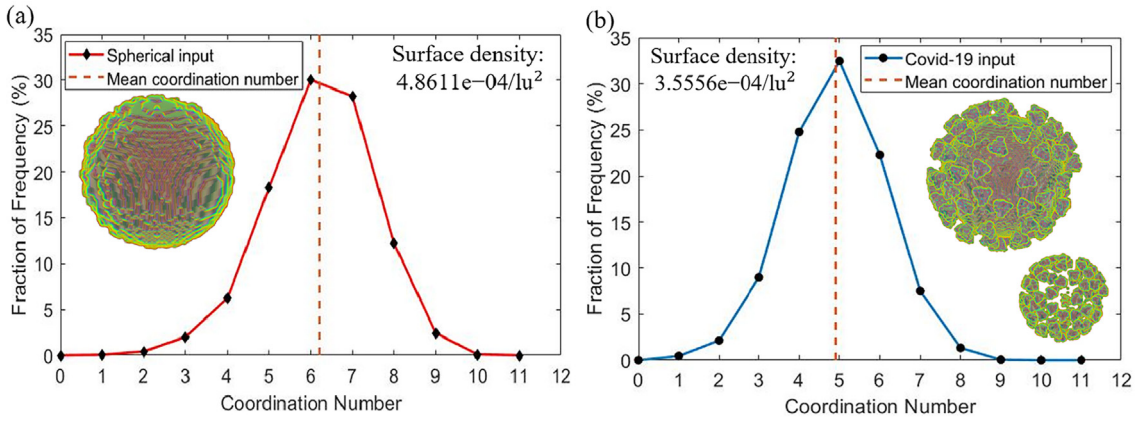

Fig. 5. Coordination number analysis and surface density measurement with (a) spherical input and (b) COVID-19 input.

agreement with the mean coordination number of the spikeless tests in this work, as shown in Fig. 5(b). However, realistic particle shape presents a modified coordination number development pattern [48]. Therefore, equivalence to the spherical analysis was located to perform a comparison with the previous spherical study. Fig. 5(b) presents the coordination number analysis and surface density measurement obtained from the virus REV-Dense cluster. The dense redistribution with COVID-19 resulted in a mean coordination number of 5 within a range of (0,11). The surface density measurement resulted in a value of $3.5556 \times 10^{-4}/lu^2$. The surface density indicates the amount of virus on the surface was 1.4610×10^{-4} per nm^2. As discussed in section 3.1, the introduction of spike structure on the spherical surface reduced the phase fraction to 62%. The corresponding result in the spherical study [42] also presents a coordination number of around 5 when the phase fraction was 62%. The above comparison indicates that the effect of introducing spike structure in individual particle shape is equivalence to reducing the packing density of the spherical cluster on the aspect of coordination number development.

The compassion between the COVID-19 input and spherical input quantitatively demonstrates the morphological difference resulted from the different assumptions. During virus cluster modelling, applying spherical assumption caused an exaggeration of the interconnection by 20% and a surface density exaggerated by 36%. The decrement of coordination number indicates that COVID-19 require a low number of interconnecting to form a structurally stable distribution. Compared with the spherical input without spike protein, the decrement in surface density from the COVID-19 cluster indicates that the same amount of virus with the spike protein can occupy an increased surface area. It can be argued that the smooth function approaches can recover the particle redistribution process through the so-called first principle. However, the inheritance of the spherical assumption will inevitably cause misleading results. The solution to model the complex geometry of the COVID-19 cluster at the current moment is the voxel-based approach, as evidenced in this study.

3.4. Fluid dynamics through virus cluster

The fundamental aim to prepare a 3D virus cluster with arbitrary redistribution is to apply these model in a digital environment for physical, chemical and biological analysis. Fig. 6 demonstrate the example application of the redistribution with a virtual permeability test. The permeation behaviour of fluid through porous media reflect the aerodynamic property of the virus cluster. Fig. 6(a) presents the virtual test with COVID-19 input, showing a stabilized fluid flow formed in 226 computational iterations with a virtual permeability of 2.23×10^{-18} m^2. In comparison, Fig. 6(b) demonstrates the permeation behaviour of fluid through a spherical cluster, showing a stabilized fluid flow formed in 205 computational iterations with a virtual permeability of 9.86×10^{-19} m^2.

Consequently, the input of COVID-19 with spike protein caused a 227% increment of the permeability and 10% decrement of stabilization rate comparing with spherical input without spike protein. Previous literature reported [49] surrounding fluid behaviour in spherical clusters with various coordination number. It was reported that the stable pressure formed by a steady flow around the cluster followed a decrement ratio when the coordination number was increased. The same reduction influence from the varied coordination numbers, which was caused by the inclusion of the surface spike, was reflected by the reduction of intrinsic permeability in the virtual test in this study. Due to the lack of relevant research, further permeability data in the precise scale level is not available from the other source upon the writing of this paper.

However, fluid behaviour comparison within the same digital environment is already enough to demonstrate the advantage of cluster modelling with surface spikes of the virus. The tremendous increment of permeability indicates that the assembled morphological difference significantly influences the aerodynamic behaviour of the virus cluster. The spike protein features the virus cluster structures, causing the increment of specific surface area. The surface area formed a transport network for the fluid flow, and an enlarged area resulted in a topologically extended length of the transport path. Consequently, the time required to form a stabilized fluid flow was extended due to the longer path. Quantitatively, the time extension introduced by the spike protein is 10% of the duration required by stabilization in a spherical cluster.

On the other hand, the increment of the permeability physically reflects that the COVID-19 cluster has lower resistivity to fluid flow than the spherical cluster. The result is consistent with the coordination number and surface density results since decreased volumetric occupation leads to increased permeability. From the aspect of solid-phase redistribution, it was concluded that the COVID-19 input led to a lower amount of particles to form a structurally stable cluster. As a result, the volumetric capacity for fluid flow is increased, leading to an enlarged cross-sectional area along the transport path for flux increment. More importantly, a morphological difference of 20% in surface density and 36% in coordination number caused a dynamical difference of 132% in permeation. The result evidence that the aerodynamic property of the virus cluster is susceptible to the local shape of a virus. It is of great necessity to strictly adopt virus input with spike protein structure in a fluid flow system, including blood fluid and airborne spread for specific types of virus. The voxel-based treatment proposed in this study is a ready solution for the above tasks.

4. Summary

The available mathematical tools for 3D particle redistribution are smooth function approaches, including MD and DEM, and voxel-based approaches based on voxel computation. The analytical geometry requirement of the smooth function approaches causes the lack of an established solution due to the complexity of the COVID-19 geometry.

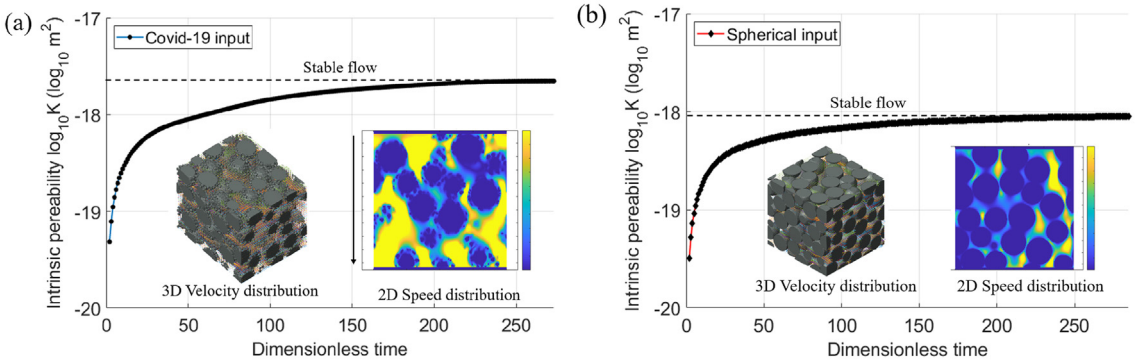

Fig. 6. (a) Virtual permeation through COVID-19 cluster. (b) Virtual permeation throug spherical cluster.

In this study, a voxel-based method to simulate the virus cluster's formation is proposed with COVID-19 input with spike protein structure. The voxel-based redistribution demonstrates the capability for arbitrary shape input and compatibility with lattice-based fluid dynamics analysis. Virus cluster modelling is an essential step for computational pathology analysis after establishing an individual virus model. The influence of morphology and detailed geometry is significant on the cluster properties and behaviour. The cluster modelling with COVID-19 input results in a 20% decrement of virus inter-contact and a 36% decrement of the surface density than the cluster modelling with spherical input. The spike protein on the virus membrane decreased the number of viruses required to form a structurally stable cluster. The compatibility between voxel-based redistribution to the LBM enables direct coupling of the cluster modelling and fluid dynamics analysis. The virtual permeation with COVID-19 input resulted in a 227% higher permeability and 10% lower stabilization rate than the same virtual test with spherical input. The virus cluster has a lower resistivity to fluid flow than the spherical cluster. The virus morphology caused a distinguish formation of the transport path through cluster in terms of effective length and cross-sectional flux area. The significant sensitivity to dynamical properties indicates that spike protein should be strictly adopted instead of roughly applying spherical assumption. The voxel-based approach is a ready-to-use solution for the automatic modelling of the COVID-19 cluster.

CRediT authorship contribution statement

Mingzhi Wang: Conceptualization, Methodology, Software, Validation, Formal analysis, Investigation, Data curation, Visualization, Writing - original draft, Writing - review & editing. **Yushi Liu**: Investigation. **Beimeng Qi**: Visualization. **Wei Wang**: Project administration.

Declaration of Competing Interest

The authors declare that they have no known competing financial interests or personal relationships that could have appeared to influence the work reported in this paper.

References

[1] L. Harper, N. Kalfa, G.M.A. Beckers, M. Kaefer, A.J. Nieuwhof-Leppink, M. Fossum, K.W. Herbst, D. Bagli, The impact of COVID-19 on research, J. Pediatr. Urol. (2020) https://doi.org/10.1016/j.jpurol.2020.07.002.

[2] E. Tagliazucchi, P. Balenzuela, M. Travizano, G.B. Mindlin, P.D. Mininni, Lessons from being challenged by COVID-19, Chaos, Solitons Fractals 137 (2020) https://doi.org/10.1016/j.chaos.2020.109923.

[3] A.C.J. de Korte, H.J.H. Brouwers, Random packing of digitized particles, Powder Technol. 233 (2013) 319–324, https://doi.org/10.1016/j.powtec.2012.09.015.

[4] X. Yang, F. Wang, Random-fractal-method-based generation of meso-model for concrete aggregates, Powder Technol. 284 (2015) 63–77, https://doi.org/10.1016/j.powtec.2015.06.045.

[5] G.T. Nolan, P.E. Kavanagh, Computer simulation of random packings of spheres with log-normaldistributions, Powder Technol. 76 (1993) 309–316, https://doi.org/10.1016/S0032-5910(05)80012-9.

[6] H. Singh, Analysis for fractional dynamics of Ebola virus model, Chaos, Solitons Fractals 138 (2020) https://doi.org/10.1016/j.chaos.2020.109992.

[7] D. Wrapp, N. Wang, K.S. Corbett, J.A. Goldsmith, C.L. Hsieh, O. Abiona, B.S. Graham, J.S. McLellan, Cryo-EM structure of the 2019-nCoV spike in the prefusion conformation, Science (80-.) 367 (2020) 1260–1263, https://doi.org/10.1126/science.aax0902.

[8] J. Rojek, A. Zubelewicz, N. Madan, S. Nosewicz, The discrete element method with deformable particles, Int. J. Numer. Methods Eng. 114 (2018) 828–860, https://doi.org/10.1002/nme.5767.

[9] D. Hou, J. Yu, P. Wang, Molecular dynamics modeling of the structure, dynamics, energetics and mechanical properties of cement-polymer nanocomposite, Compos. Part B Eng. 162 (2019) 433–444, https://doi.org/10.1016/j.compositesb.2018.12.142.

[10] F.P. Di Maio, A. Di Renzo, Modelling particle contacts in distinct element simulations: linear and non-linear approach, Chem. Eng. Res. Des. 83 (2005) 1287–1297, https://doi.org/10.1205/cherd.05089.

[11] M. Dorn, D. Hekmat, Simulation of the dynamic packing behavior of preparative chromatography columns via discrete particle modeling, Biotechnol. Prog. 32 (2016) 363–371, https://doi.org/10.1002/btpr.2210.

[12] K. Kildashti, K. Dong, B. Samali, Explicit force model for discrete modelling of elliptical particles, Comput. Geotech. 110 (2019) 122–131, https://doi.org/10.1016/j.compgeo.2019.02.004.

[13] B. Smeets, T. Odenthal, S. Vanmaercke, H. Ramon, Polygon-based contact description for modeling arbitrary polyhedra in the discrete element method, Comput. Methods Appl. Mech. Eng. 290 (2015) 277–289, https://doi.org/10.1016/j.cma.2015.03.004.

[14] C.P. Koch, M. Lemeshko, D. Sugny, Quantum control of molecular rotation, Rev. Mod. Phys. 91 (2019) https://doi.org/10.1103/RevModPhys.91.035005.

[15] M. Dadkhah, M. Peglow, E. Tsotsas, Characterization of the internal morphology of agglomerates produced in a spray fluidized bed by X-ray tomography, Powder Technol. 228 (2012) 349–358, https://doi.org/10.1016/j.powtec.2012.05.051.

[16] R. Pashminehazar, S.J. Ahmed, A. Kharaghani, E. Tsotsas, Spatial morphology of maltodextrin agglomerates from X-ray microtomographic data: Real structure evaluation vs. spherical primary particle model, Powder Technol. 331 (2018) 204–217, https://doi.org/10.1016/j.powtec.2018.03.008.

[17] A. Sternberg, C. Naujokat, Structural features of coronavirus SARS-CoV-2 spike protein: Targets for vaccination, Life Sci. 257 (2020) https://doi.org/10.1016/j.lfs.2020.118056.

[18] T. Byholm, M. Toivakka, J. Westerholm, Effective packing of 3-dimensional voxel-based arbitrarily shaped particles, Powder Technol. 196 (2009) 139–146, https://doi.org/10.1016/j.powtec.2009.07.013.

[19] M. Wang, A. Al-Tabbaa, W. Wang, Improving discrete particle packing models for the microstructural formation simulation of Portland cement, Constr. Build. Mater. 229 (2019) 116841, https://doi.org/10.1016/j.conbuildmat.2019.116841.

[20] X. Jia, R. Williams, A packing algorithm for particles of arbitrary shapes, Powder Technol. 120 (2001) 175–186, https://doi.org/10.1016/S0032-5910(01)00268-6.

[21] A. Zubov, J.F. Wilson, M. Kroupa, M. Šoóš, J. Kosek, Numerical modeling of viscoelasticity in particle suspensions using the discrete element method, Langmuir. 35 (2019) 12754–12764, https://doi.org/10.1021/acs.langmuir.9b01107.

[22] J.J. D'Arruda, High-temperature quantum corrections to the second virial coefficient for a hard-core-plus-attractive-well-potential model, Phys. Rev. A 7 (1973) 820–822, https://doi.org/10.1103/PhysRevA.7.820.

[23] S. Nandy, A. Barthakur, Pairwise three soliton interactions, soliton logic gates in coupled nonlinear Schrödinger equation with variable coefficients, Commun. Nonlinear Sci. Numer. Simul. 69 (2019) 370–385, https://doi.org/10.1016/j.cnsns.2018.10.011.

[24] M. Poursina, P.E. Nikravesh, Optimal damping coefficient for a class of continuous contact models, Multibody Syst. Dyn. (2020) https://doi.org/10.1007/s11044-020-09745-x.

[25] Y. Li, H. Jiang, Elastic modulus prediction of particle reinforced composites based on sphere model, IOP Conf. Ser. Mater. Sci. Eng. 733 (2020) https://doi.org/10.1088/1757-899X/733/1/012032.

[26] J.L. Osa, N. Ortega, G. Vidal, B. Fernandez-Gauna, A. Carballo, I. Tolosa, Future of the discrete element method in the modelling of grinding wheels, Eng. Comput. (Swansea, Wales) 35 (2018) 2255–2271, https://doi.org/10.1108/EC-11-2017-0450.

[27] A.K. Singh, E. Tsotsas, Stochastic model to simulate spray fluidized bed agglomeration: a morphological approach, Powder Technol. 355 (2019) 449–460, https://doi.org/10.1016/j.powtec.2019.07.075.

[28] A.K. Singh, E. Tsotsas, A tunable aggregation model incorporated in Monte Carlo simulations of spray fluidized bed agglomeration, Powder Technol. 364 (2020) 417–428, https://doi.org/10.1016/j.powtec.2020.02.016.

[29] Z.T. Al-Sharify, T.A. Al-Sharify, N.T. Al-Sharify, H.Y. Naser, A critical review on medical imaging techniques (CT and PET scans) in the medical field, IOP Conf. Ser. Mater. Sci. Eng. 870 (2020) https://doi.org/10.1088/1757-899X/870/1/012043.

[30] J. von Neumann, The general and logical theory of automata, in: L.A. Jeffress (Ed.), Syst. Res. Behav. Sci. A Sourceb, John Wiley & Sons, New York 2017, pp. 97–107.

[31] I. Chenn, I.M. Sigal, On derivation of the Poisson–Boltzmann equation, J. Stat. Phys. 180 (2020) 954–1001, https://doi.org/10.1007/s10955-020-02562-8.

[32] L.M. Brieger, E. Bonomi, A stochastic cellular automaton model of non-linear diffusion and diffusion with reaction, J. Comput. Phys. 94 (1991) 467–486, https://doi.org/10.1016/0021-9991(91)90231-9.

[33] U. Frisch, D. D'Humières, B. Hasslacher, P. Lallemand, Y. Pomeau, J.-P. Rivet, Lattice gas hydrodynamics in two and three dimensions, Complex Syst. 1 (1987) 649–707, http://www.complex-systems.com/abstracts/v01_i04_a07.html.

[34] S. Ponce Dawson, S. Chen, G.D. Doolen, Lattice Boltzmann computations for reaction-diffusion equations, J. Chem. Phys. 98 (1993) 1514, https://doi.org/10.1063/1.464316.

[35] I.M. Gitman, M.B. Gitman, H. Askes, Quantification of stochastically stable representative volumes for random heterogeneous materials, Arch. Appl. Mech. 75 (2006) 79–92, https://doi.org/10.1007/s00419-005-0411-8.

[36] N. Ukrainczyk, E.A.B. Koenders, Representative elementary volumes for 3D modeling of mass transport in cementitious materials, Model. Simul. Mater. Sci. Eng. 22 (2014) 35001, https://doi.org/10.1088/0965-0393/22/3/035001.

[37] National Institutes of Health, 3D model of the Covid-19 virus, Proteins, Macromol. Viruses (2020) https://3dprint.nih.gov/discover/3DPX-013270 (accessed September 25, 2020).

[38] Z. Varga, A.J. Flammer, P. Steiger, M. Haberecker, R. Andermatt, A. Zinkernagel, M.R. Mehra, F. Scholkmann, R. Schüpbach, F. Ruschitzka, H. Moch, Electron microscopy of SARS-CoV-2: a challenging task – Authors' reply, Lancet. 395 (2020), e100, https://doi.org/10.1016/S0140-6736(20)31185-5.

[39] K. Suga, Y. Kuwata, K. Takashima, R. Chikasue, A D3Q27 multiple-relaxation-time lattice Boltzmann method for turbulent flows, Comput. Math. Appl. 69 (2015) 518–529, https://doi.org/10.1016/j.camwa.2015.01.010.

[40] R. Chisholm, S. Maddock, P. Richmond, Improved GPU near neighbours performance for multi-agent simulations, J. Parallel Distrib. Comput. 137 (2020) 53–64, https://doi.org/10.1016/j.jpdc.2019.11.002.

[41] M. Wang, Numerical Modelling of the Kinetics and Microstructural Development of Carbonated Magnesia-Based Cements (Doctoral Dissertation), University of Cambridge, 2017.
[42] R.M. German, Coordination number changes during powder densification, Powder Technol. 253 (2014) 368–376, https://doi.org/10.1016/j.powtec.2013.12.006.
[43] J.P. Boon, The Lattice Boltzmann Equation for Fluid Dynamics and Beyond, 2003 https://doi.org/10.1016/s0997-7546(02)00005-5.
[44] M. Wang, Y. Liu, B. Qi, A. Al-Tabbaa, W. Wang, Percolation and conductivity development of the rod networks within randomly packed porous media, Compos. Part B Eng. 187 (2020) 107837, https://doi.org/10.1016/j.compositesb.2020.107837.
[45] C. Song, P. Wang, H.A. Makse, A phase diagram for jammed matter, Nature 453 (2008) 629–632, https://doi.org/10.1038/nature06981.
[46] J.M. Valverde, A. Castellanos, Random loose packing of cohesive granular materials, Europhys. Lett. 75 (2007) 985–991, https://doi.org/10.1209/epl/i2006-10208-4.
[47] D. He, N.N. Ekere, L. Cai, Computer simulation of random packing of unequal particles, Phys. Rev. E Stat. Phys. Plasmas Fluids Relat. Interdiscip. Topics 60 (1999) 7098–7104, http://www.ncbi.nlm.nih.gov/pubmed/11970649.
[48] A. Karamchandani, H. Yi, V.M. Puri, MicroCT imaging to determine coordination number and contact area of biomass particles in densified assemblies, Powder Technol. 354 (2019) 466–475, https://doi.org/10.1016/j.powtec.2019.06.002.
[49] M. Kamyabi, K. Saleh, R. Sotudeh-Gharebagh, R. Zarghami, Effects of the number of particles and coordination number on viscous-flow agglomerate sintering, Particuology. 43 (2019) 76–83, https://doi.org/10.1016/j.partic.2018.01.015.